

Evaluating Sulfur as a P-Type Dopant in Cu₃N Using Ab Initio Methods

Sajjad A. Alqunais, Md Maidul Islam,* Bishal B. Dumre, Sanjay V. Khare, and Daniel G. Georgiev

Copper nitride (Cu₃N) is an environmentally friendly semiconducting material with bipolar doping capability and is of interest to various applications. As deposited Cu₃N films have inherent n-type conductivity, further controllable n-type doping is possible by introducing metal impurities. First-principles methods based on density functional theory and beyond have been employed to study the p-type doping behavior of sulfur atoms in Cu₃N. The structural, electronic, optical, and thermal properties of pure Cu₃N and sulfur-doped Cu₃N are computed for single and 3 × 3 × 3 supercells. Sulfur doping causes a shift from intrinsic n-type to p-type behavior. This study confirms that sulfur atoms in sulfur-doped copper nitride preferentially occupy interstitial positions over nitrogen substitution, face-centered, or copper substitution sites. Due to this change and an increased lattice constant, Cu₃N becomes a softer material with a larger bandgap in the single-cell alloy. Doped Cu₃N supercell results show significant changes in optical properties appropriate for solar and other photoelectric applications. Cu₃N:S exhibits remarkable enhancements in power factor and thermal and electrical conductivity, indicating potentially better performance in thermoelectric applications. The dielectric constant and absorption coefficient also significantly change with the incorporation of sulfur into Cu₃N.

for fabricating a homogeneous junction that can aid in band alignment and carrier transportation in a device structure, thereby enhancing the conversion efficiency.^[3,4] Cu₃N also has an optical absorption onset that aligns with the solar spectrum.^[5] Its earth-abundant, low-cost, and nontoxic elemental composition and tunable bandgap ranging from 0.8 to 1.9 eV makes it a promising candidate for applications in electronic devices, optical devices, and solar cells.^[4–9] Notably, a large range of reported values for the Cu₃N bandgap arises from deposition parameters,^[10–13] which influence the copper-to-nitrogen (Cu-to-N) ratio and, consequently, the material's structure.^[9,14–16]

The conductivity type of Cu₃N is influenced by its Cu-to-N ratio, where a higher Cu content results in n-type conductivity and a higher N content leads to p-type conductivity.^[2,4] Previous research has emphasized the critical role of native point defects, such as copper interstitials (Cu_i) and copper vacancies (V_{Cu}), combined with the Fermi-level position in determining the conductivity of Cu₃N films.^[2,6] Hence, varying

the Cu-to-N ratio to achieve the desired conductivity type may lead to an undesirable accumulation of native point defects and diminishing device performance due to defect states in the Cu₃N absorber layer inhibiting carrier transport (Shockley–Read–Hall recombination).^[6]

Such limitations can be overcome by doping. The intentional introduction of impurities for the purpose of doping Cu₃N is a critical area of study as it provides an opportunity to modify electronic properties and influence crystallinity, mobility, resistivity, absorption, thermal stability, and growth orientation. In the past, various other dopants and their behaviors have been explored across a wide range of options, including main group metals, transition metals, lanthanides, and even nonmetals.^[17–26] For example, a photodetector designed by doping Cu₃N with Mn had a doubly faster photocurrent response than the undoped photodetector.^[27] Similarly, introducing N in the body-centered site of Cu₃N resulted in a reduced bandgap of 1.1 eV and improved photocurrent density (1.66 mA cm^{−2} at 10 V) compared to undoped Cu₃N.^[28] A first-principles study of 3d-transition metal-doped Cu₃N revealed its ability to transition from semiconducting to metallic.^[29]


Remarkably, the majority of experimental doping attempts yield n-type or metallic behavior, with Cu₃N itself being

1. Introduction

The relentless pursuit of faster, more efficient, environmentally friendly, and cost-effective semiconductor materials has fueled extensive research efforts to discover novel materials capable of fulfilling these demands for various applications. Among these promising materials, transition metal nitrides, particularly copper nitride (Cu₃N), are intriguing candidates because of the observed bipolar doping.^[1,2] This property is advantageous

S. A. Alqunais, M. M. Islam, D. G. Georgiev
Department of Electrical Engineering and Computer Science
University of Toledo
Toledo, OH 43606, USA
E-mail: mdmaidul.islam@rockets.utoledo.edu

B. B. Dumre, S. V. Khare
Department of Physics and Astronomy, and Wright Center for
Photovoltaics Innovation and Commercialization (PVIC)
University of Toledo
Toledo, OH 43606, USA

 The ORCID identification number(s) for the author(s) of this article can be found under <https://doi.org/10.1002/pssb.202400336>.

DOI: 10.1002/pssb.202400336

inherently an n-type semiconductor.^[3,17] Therefore, researchers are actively seeking an effective p-type dopant, considering the benefits of creating a homojunction. Specifically, due to its bipolar capability and highly symmetric hole, and electron mobilities, copper nitride can be used in many applications where nontoxic and environmentally friendly oxide semiconductors have failed to meet specific requirements.^[30] A recent report showed that using fluorine (F) as a p-type dopant in Cu₃N resulted in a high hole mobility of 45–81 cm² V⁻¹ s⁻¹,^[3] which is greater than that of cutting-edge p-type GaN (30–40 cm² V⁻¹ s⁻¹).^[31] The device performance experimentally found was acceptable.^[30] However, considering the toxicity of fluorine and related compounds, this approach does not provide a solution for the objective of a nontoxic, environmentally friendly process for accessing copper nitride semiconductor precursors.^[3,32] Additionally, iodine, belonging to the same VII group, serves as a potential p-type dopant with hole densities ranging from 10¹⁶ to 10¹⁷ cm⁻³. However, its use leads to shallow-like acceptors, causing the device to experience significant indirect recombination.^[33] An intuitive choice for doping Cu₃N is to replace N with carbon (C) to realize p-type doping, as C has one fewer electron than N.^[3] However, C can form a deep acceptor level with a thermal activation energy of 0.3 eV.^[34] Another approach is to introduce atoms with appropriate properties at interstitial sites. An interstitial atom with remarkably high electronegativity can form a shallow acceptor level as a dopant that gives rise to p-type conductivity.^[3]

After carefully reviewing the literature, we concluded that the study of doping Cu₃N with sulfur (S), a highly electronegative atom,^[35] is lacking in the literature. Therefore, this work examines the possibility of doping Cu₃N by p-type dopants by introducing sulfur. This study is based on the principles of density functional theory (DFT) and aims to investigate the structural and electronic traits of introducing sulfur in Cu₃N and the impact on the Fermi-level positioning within Cu₃N. We examined the effectiveness of the dopant in enhancing the p-type conductivity of Cu₃N and potentially improving its performance in various applications.

2. Computational Methods

In this work, the Quantum Open-Source Package for Research in Electronic Structure, Simulation, and Optimization (Quantum ESPRESSO, abbr. QE), thermo_pw, and BoltzTraP^[36–39] were used as computational DFT tools to investigate the structural, electronic, optical, and thermal properties of pure Cu₃N and sulfur-doped Cu₃N (Cu₃N:S) at two different cell sizes, where a single cell is an alloying condition and a 3 × 3 × 3 supercell is a doping condition. The DFT calculations were performed using the SSSP_1.1.2_PBE_efficiency pseudopotential library.^[40] The calculations converged at $ecutrho = 350$ Ry, $ecutwfc = 40$ Ry, $conv_thr = 10^{-6}$ Ry,^[41–44] and k -points = 8 × 8 × 8^[45–49] for Cu₃N and Cu₃N:S, respectively.

The calculations for intrinsic Cu₃N were performed in an anti-ReO₃ cubic cell (space group $Pm\bar{3}m$), and for Cu₃N:S, a sulfur atom was incorporated somewhere in the center of the cubic cell depending on the type of defective dopant. The mechanical and dielectric properties were subsequently determined using thermo_pw, and higher cutoffs were used to obtain accurate results,

viz. $ecutrho = 460$ Ry, $ecutwfc = 78$ Ry, $conv_thr = 10^{-12}$ Ry, and k -points = 12 × 12 × 12.^[50–54] Supercells of both intrinsic and doped Cu₃N were relaxed. The outputs of non-self-consistent calculations were used in BoltzTraP to determine the electronic and thermal properties.^[55–60] These properties were deduced using the outputs of the relaxed supercell nonself-consistent QE calculations in BoltzTraP.

Hubbard U correction calculations were performed to estimate the hybrid functional results. A correction value of $U = 7.64$ eV was used, similar to what Zervos et al.^[61] applied for the Cu $3d$ state in all Hubbard calculations. The cutoff energies were the same.

The formation energies were calculated by performing optimized and relaxed calculations for the unit cells and supercells.^[62–65] The ground-state energies of bulk Cu₃N, Cu₃N:S, copper, sulfur, and nitrogen were calculated to determine the formation energies:

$$E^f = E_{tot}^{Cu_3N:S} - E_{tot}^{Cu} - E_{tot}^N - E_{tot}^S \quad (1)$$

$$E^f = E_{tot}^{Cu_3N:S} - E_{tot}^{Cu_3N} - E_{tot}^S \quad (2)$$

where $E_{tot}^{Cu_3N}$ is the total ground-state energy of Cu₃N, E_{tot}^{Cu} is the total ground-state energy of Cu atoms, E_{tot}^N is the total ground-state energy of N atoms, and E_{tot}^S is the total ground-state energy of S atoms. Fcc Cu (space group: $Fm\bar{3}m$), orthorhombic sulfur (space group: $Pnnm$), and a nitrogen molecule in a large box ($a = 11.1$ Å) were used to determine the total energy of the elements. The formation energy is generally discussed in two separate cases. In Equation (1), we consider growing or depositing the unit cell alloy Cu₃N:S from scratch. In Equation (2), we considered having a bulk pure Cu₃N supercell and then doped it with a sulfur atom, for example, using ion implantation. We utilized Equation (2) in our results to model the case where ion implantation is usually carried out in a research setting rather than creating the material from scratch. The formation energy was determined for four different doping sites in the supercell to determine which site is most likely to form in the laboratory.

Using thermo_pw, we calculated the elastic, vibrational, mechanical, and optical properties of Cu₃N and Cu₃N:S. The code calculates the mechanical properties using the Voigt–Reuss–Hill scheme. The time-dependent density functional perturbation theory and the Lanczos chain algorithm were used to determine the optical properties.

One important clarification is that, in certain situations, the distinction between alloys and doped semiconductors is not always clear and is alternatively used.^[66] This ambiguity is particularly true for DFT analysis, where larger system analyses are not feasible. In this study, both alloying and doping are used interchangeably, although in practical applications, this would be regarded as alloying (because doping is typically performed at the parts per million level of impurity). However, considering the objective of this analysis to understand the effect of sulfur impurities on the semiconductor characteristics of Cu₃N, this difference is not a significant factor.

3. Results and Discussion

Based on the DFT analysis, the effect of sulfur doping on the structural, elastic, electronic, and thermal properties of Cu_3N is discussed as follows.

3.1. Structural Properties

The structures of Cu_3N and $\text{Cu}_3\text{N}:\text{S}$ are shown in **Figure 1a,b** and were optimized by finding the minimum ground-state total energy of different unit cell volumes. **Figure 2** shows the results of the total energies as a function of volume for both the Cu_3N and $\text{Cu}_3\text{N}:\text{S}$ unit cells. The curve was obtained by using the Birch–Murnaghan equation of state (EoS).^[67] The calculated parameters are summarized in **Table 1**. The lattice constant is $\approx 3.83 \text{ \AA}$, which is similar to the reports that have been published.^[68–71] For the doped unit cell, there is an increase in the lattice constant of $\approx 0.136 \text{ \AA}$, resulting in a lattice constant of 3.96 \AA . This increment in the lattice constant can be attributed to the insertion of a totally new atom of sulfur in a void.

The formation energy of an alloyed Cu_3N single cell, as shown in **Table 1**, indicates that the alloy can be formed in the laboratory. **Table 2** summarizes the four doping configurations for the doping situation of the supercell. The following four doping sites were considered to determine the most likely site to form in the laboratory: S_i , S_N , S_{Cu} , and S_{Face} , that is, the interstitial site, substituting a nitrogen atom, replacing a copper atom, and in the boundary face of the middle cell, respectively. It can be concluded that the interstitial site has the lowest E_f^f ; thus, it is the most likely to form. Our further discussion in the article will now focus on this interstitial S-doped Cu_3N when we report it

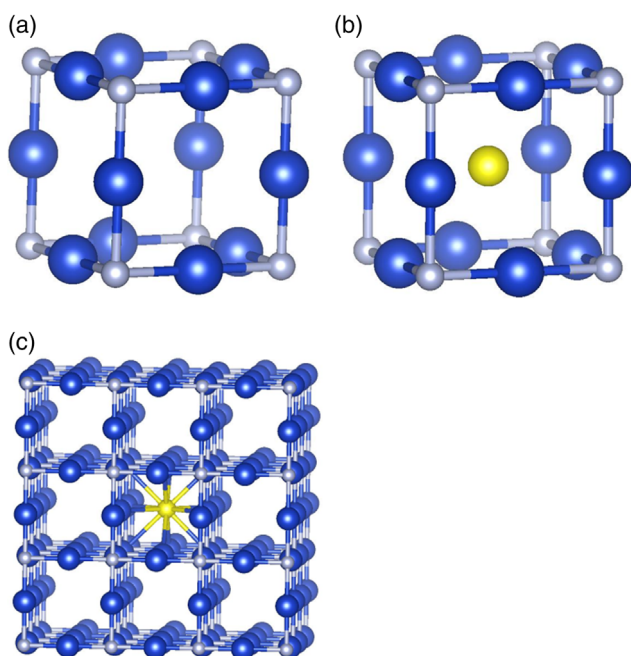


Figure 1. a) Intrinsic Cu_3N single, b) $\text{Cu}_3\text{N}:\text{S}$ single cell, and c) $\text{Cu}_3\text{N}:\text{S}$ $3 \times 3 \times 3$ supercell. Silver, blue, and yellow represent nitrogen, copper, and sulfur atoms, respectively. These figures are obtained using Visualization for Electronic and STructural Analysis (VESTA).^[76]

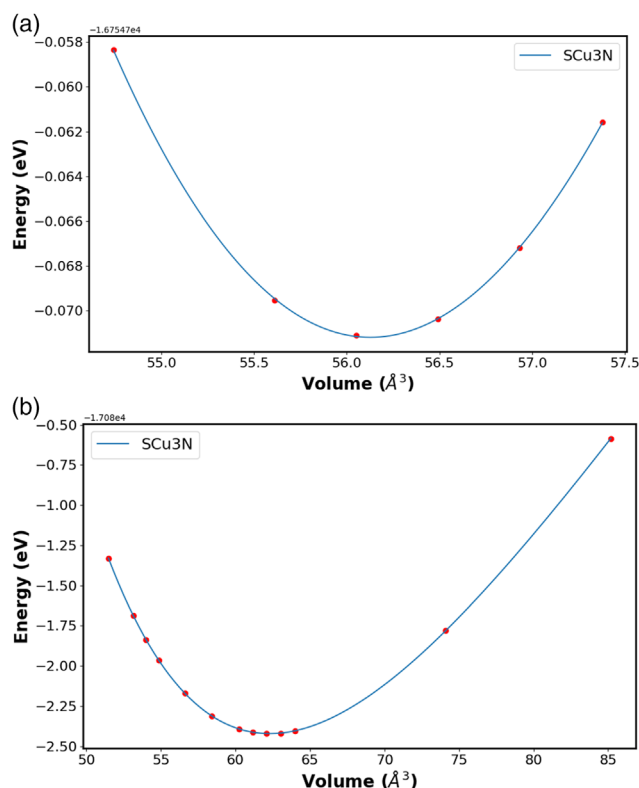


Figure 2. Total energy (Ry) versus cell volume (\AA^3) for a) Cu_3N and b) $\text{Cu}_3\text{N}:\text{S}$ single cells.

Table 1. Calculated lattice constant (a) using the birch–murnaghan EoS, bulk modulus (B), shear modulus (G), young’s modulus (E), Poisson’s ratio (n), and formation energy (E_f) of intrinsic and alloyed single cells.

	a [\AA]	B^a [GPa]	G [GPa]	E [GPa]	n	E_f^f [eV]
Cu_3N	3.828664	114.726	37.315	100.319	0.344	–
$\text{Cu}_3\text{N}:\text{S}$	3.964257	128.709	12.577	36.401	0.447	–1.363

^a) B , G , E , and n were deduced by the Voigt–Reuss–Hill scheme using thermo_pw.

Table 2. Formation energies (E_f^f) and Seebeck coefficients (S) of doped and undoped $3 \times 3 \times 3$ Cu_3N supercells. S_i , S_N , S_{Face} , and S_{Cu} are sulfur atoms with a subscript indicating the doping site.

	Undoped	S_i	S_N	S_{Face}	S_{Cu}
E_f^f [eV]	–	–1.8869265	–0.9660077	–0.3584735	0.40630146
S_{xx} [mV K^{-1}]	–2.33	107.59	–27.74	23.75	65.57
S_{yy} [mV K^{-1}]	–2.33	107.59	–27.74	23.75	130.74
S_{zz} [mV K^{-1}]	–2.33	107.59	–27.74	–76.31	130.74

as a doped material unless otherwise stated. Notably, oxygen from the same periodic table group has different formation energy; it has the lowest formation energy at the nitrogen site compared to sulfur.^[3,72,73] Furthermore, oxygen at the interstitial site also results in p-type Cu_3N .^[73]

3.2. Elastic Properties

Using thermo_pw, the elastic properties of the Cu_3N and $\text{Cu}_3\text{N}:\text{S}$ unit cells were calculated. The algorithm calculates the elastic constants and other mechanical properties by applying stresses and strains at different points. The results can be seen in Table 1 and 3 and are in good agreement with what has been published.^[71,74] Incorporating sulfur into Cu_3N significantly decreased the elastic constants C_{11} and C_{44} but substantially increased C_{12} . The material is in line with the mechanical stability conditions $C_{11} > |C_{12}|$, $C_{44} > 0$, $B = (C_{11} + 2C_{12})/3 > 0$, and $C_{12} < B < C_{11}$. Thus, $\text{Cu}_3\text{N}:\text{S}$ is mechanically stable.

The bulk modulus and Poisson's ratio increase in the alloy. Nevertheless, there are significant decreases in the shear and Young's modulus, indicating that $\text{Cu}_3\text{N}:\text{S}$ is softer than Cu_3N and can deform more easily but is not as compressible. Table 4 summarizes the sound velocities and Debye temperatures of Cu_3N and $\text{Cu}_3\text{N}:\text{S}$.

3.3. Electronic Properties

The electronic properties of both single cells and super cells of $\text{Cu}_3\text{N}:\text{S}$ were examined. The projected density of states (PDOS) of the $\text{Cu}_3\text{N}:\text{S}$ single-cell alloy is shown in Figure 3. Figure 3a shows that the incorporation of sulfur decreases the Fermi level under the valence band. When a charge of -2 was added to the alloy (Figure 3b), the Fermi level shifted to the middle of the gap. This also signifies that sulfur with two electrons deficient in its final shell can transfer those electrons in its orbit, thereby creating a deficiency in available electrons. As sulfur is a widely known highly electronegative atom, it is able to attract electrons more into the core of the orbit rather than releasing them as free electrons. When a sulfur atoms is added into the interstitial space, more electrons are contained than released, forcing a p-type feature. This result indicated that sulfur has the potential for p-type doping of Cu_3N . The same calculations were performed using the Hubbard functional, which has widened the gap (Figure S1, Supporting Information). Figure 4a shows the PDOS for the sulfur-doped Cu_3N supercell. The Fermi level shifted slightly below the valence band due to the doping of

Table 3. Calculated elastic constants and compliances of intrinsic and alloyed Cu_3N single cells.

Single	C_{11} [GPa]	C_{12} [GPa]	C_{44} [GPa]	S_{11} (1/GPa)	S_{12} (1/GPa)	S_{44} (1/GPa)
Cu_3N	236.544	53.817	18.404	0.00462	-0.00086	0.0543
$\text{Cu}_3\text{N}:\text{S}$	174.748	105.689	5.376	0.01052	-0.00396	0.1860

Table 4. Calculated sound velocities and Debye temperature, where (V_p) is the compressional sound velocity, (V_B) is the bulk sound velocity, (V_C) is the shear sound velocity, (V_D) is the average Debye sound velocity, and (Q_D) is the Debye temperature.

	V_p [m s^{-1}]	V_B [m s^{-1}]	V_C [m s^{-1}]	V_D [m s^{-1}]	Q_D [K]
Cu_3N	5211.962	4352.877	2482.491	2606.853	321.803
$\text{Cu}_3\text{N}:\text{S}$	4801.970	4516.733	1411.925	1477.270	189.740

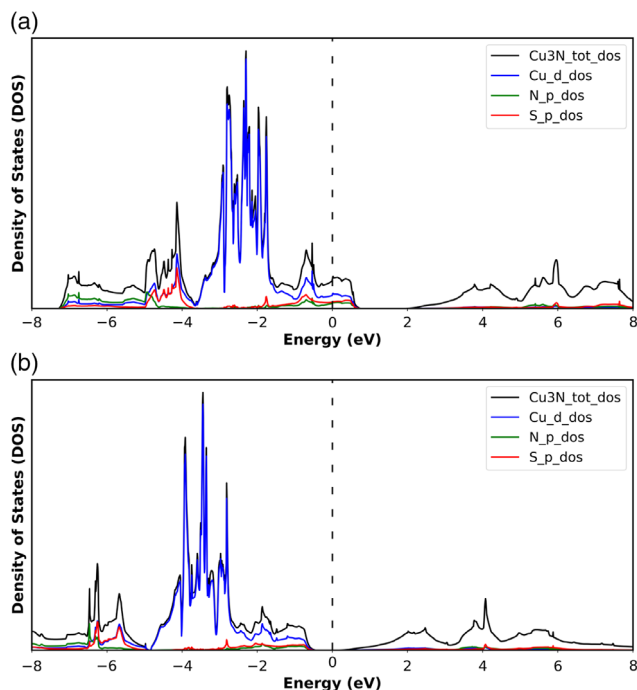


Figure 3. PDOS of a $\text{Cu}_3\text{N}:\text{S}$ single cell: a) intrinsic and b) -2 charged.

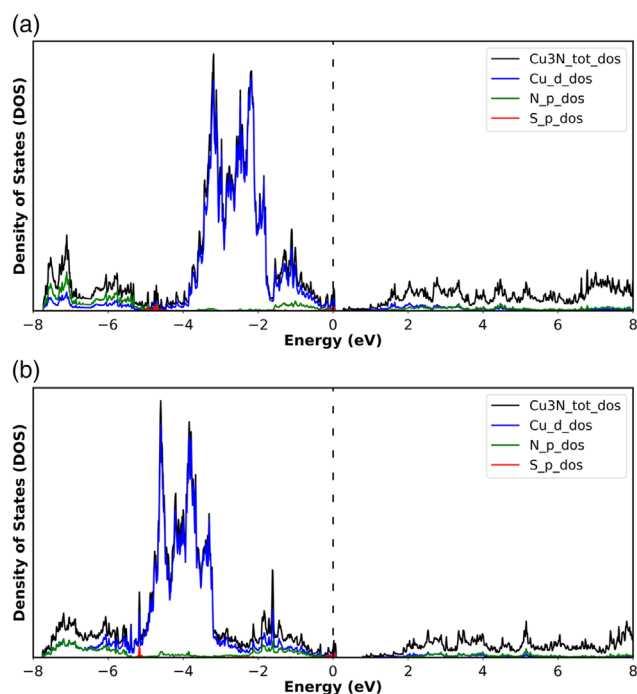


Figure 4. PDOS for $3 \times 3 \times 3$ $\text{Cu}_3\text{N}:\text{S}$: a) PBE and b) PBE + Hubbard $U = 7.64$ eV.

sulfur, a similar result to what we observed in the single-cell calculation in Figure 3. Figure 4b shows the PDOS obtained using the Hubbard parameter to obtain a gap close to the more accurate experimental results. Immediately below the Fermi level in the

valence band, Cu *d*-states dominate over other elements in both single-cell and supercell calculations. There is no sign that Cu dominates the DOS above the Fermi level; all the atoms contribute equally.

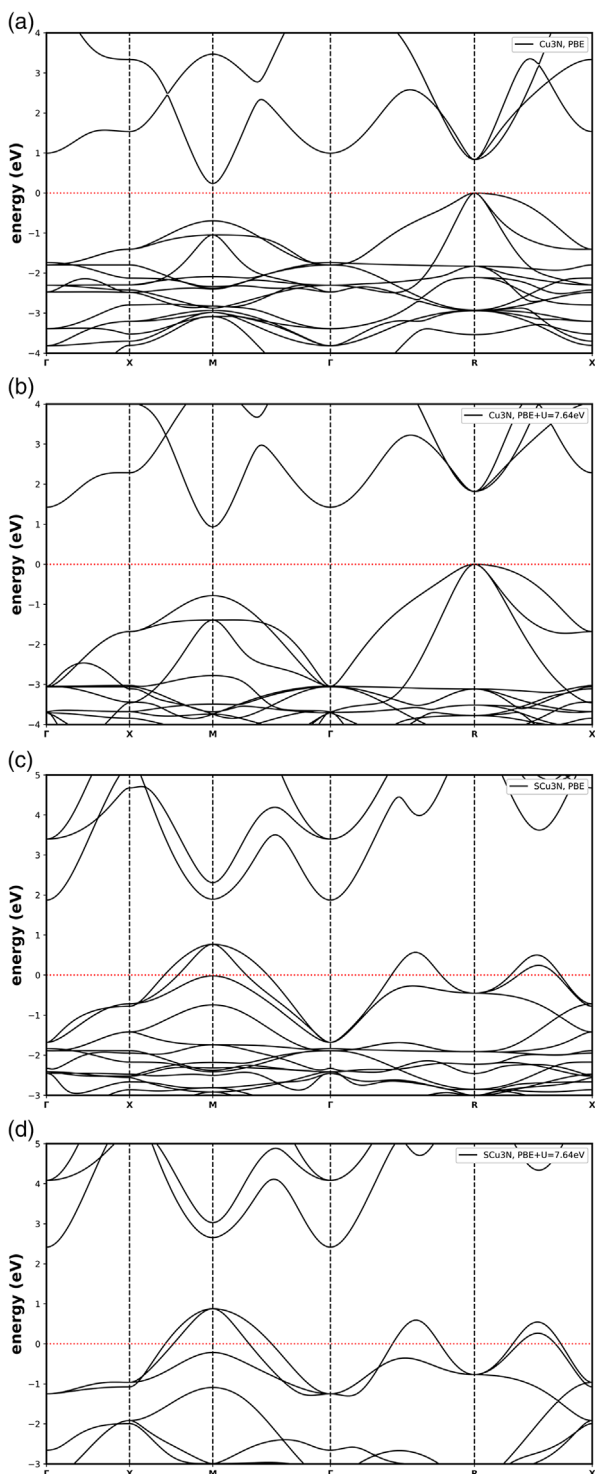


Figure 5. Band structure of intrinsic and alloyed Cu_3N single cells: a) pure Cu_3N , b) pure $\text{Cu}_3\text{N} + U$, c) sulfur-alloyed Cu_3N , and d) sulfur-alloyed $\text{Cu}_3\text{N} + U$.

3.3.1. Single Cell

In this section, a single cell, the primary unit of analysis, is used to simulate the properties of Cu_3N . The effect of incorporating sulfur into the supercell Cu_3N will be discussed in the next section.

Band Structure: Figure 5a shows the undoped single-cell band structure, which aligns with the results of other calculations in the literature.^[5,6,11,29,64–66,69] The bandgaps are 0.2364, 0.931, and 0.8369 eV for the high-symmetry points R–M, M–M, and R–R, respectively. A value of 7.64 eV for the Hubbard functional

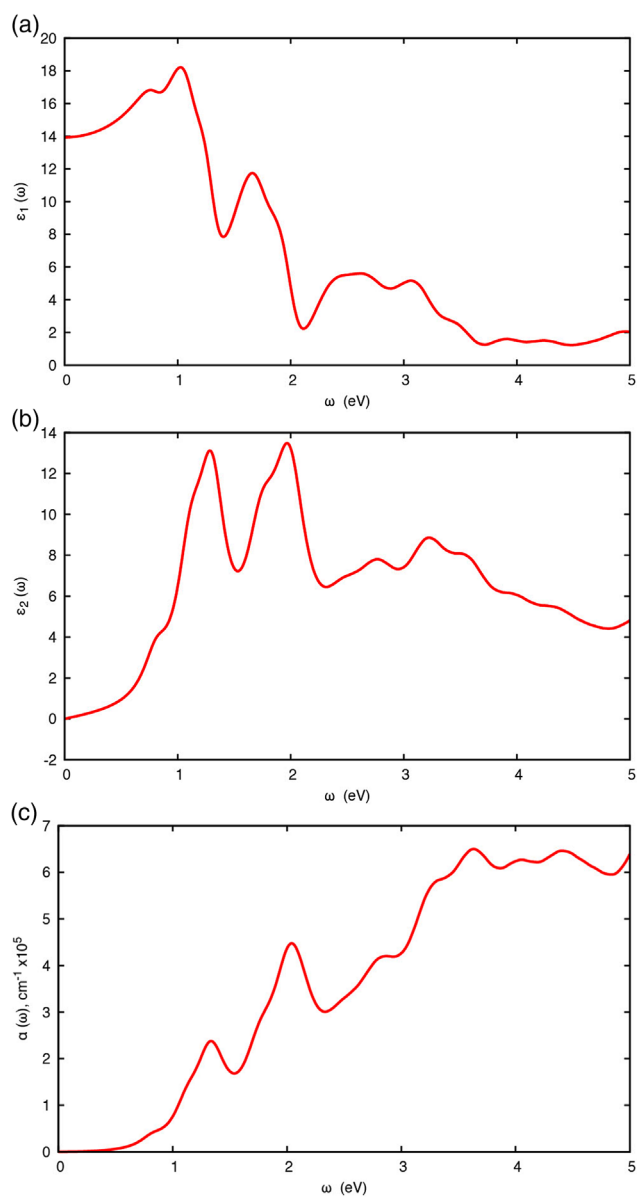


Figure 6. Optical properties of Cu_3N and $\text{Cu}_3\text{N}:\text{S}$ single cells: a) real part of the dielectric constant Cu_3N , b) imaginary part of the dielectric constant Cu_3N , c) absorption coefficient of Cu_3N , d) real part of the dielectric constant $\text{Cu}_3\text{N}:\text{S}$, e) imaginary part of the dielectric constant $\text{Cu}_3\text{N}:\text{S}$, and f) absorption coefficient of $\text{Cu}_3\text{N}:\text{S}$.

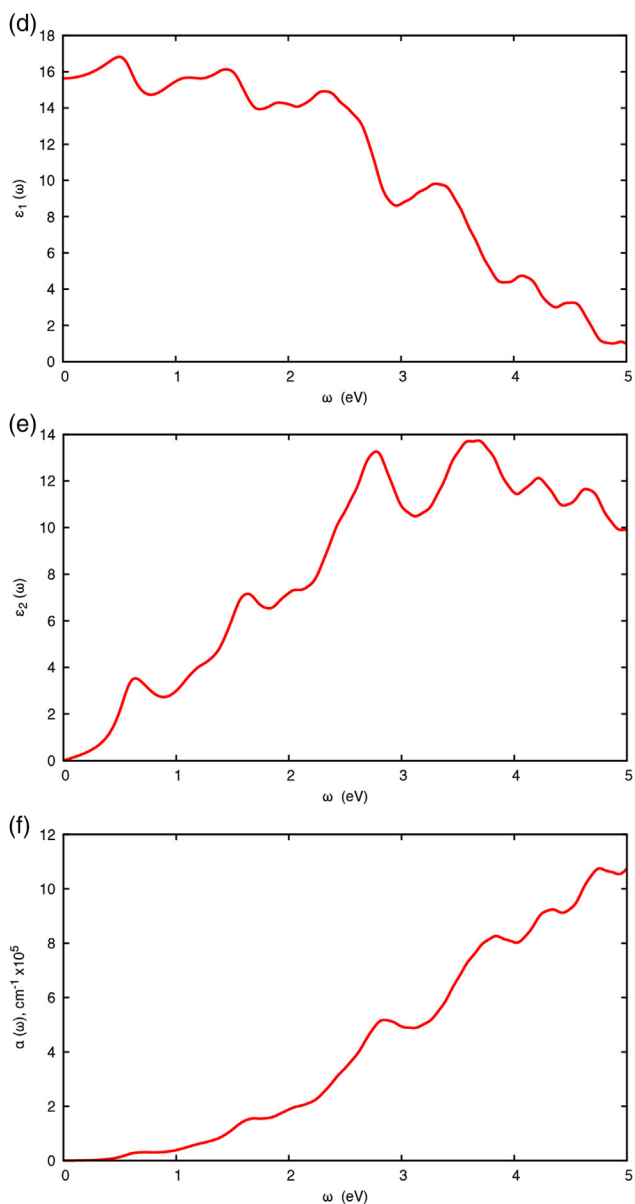


Figure 6. Continued.

was used for copper, similar to what Zervos et al. used in their Hubbard calculation to estimate a bandgap similar to the Heyd-Scuseria-Ernzerhof functional.^[61,69] We produced a similar band structure with this value (Figure 5b). The bandgaps obtained utilizing Hubbard are 0.9369, 1.7182, and 1.8177 eV for the high-symmetry points R–M, M–M, and R–R, respectively.

Figure 5c shows the band structure for the alloy $\text{Cu}_3\text{N:S}$, which has a band structure different from that of Cu_3N . Due to the incorporation of sulfur, the band structure changes, and the Fermi level drops below the valence band, indicating a degenerate p-type semiconductor similar to the incorporation of oxygen at the interstitial site.^[73] The $\text{Cu}_3\text{N:S}$ alloy has a different band structure with different bandgaps and high symmetry

transitions, 1.1260 and 1.1050 eV for M–M and M–G, respectively. We also used Hubbard for this alloy to better predict the bandgap, 1.7762 eV and 1.5372 for M–M and M–G, respectively. These bandgap values and optical properties, discussed in the next section, indicate that Cu_3N and $\text{Cu}_3\text{N:S}$ are suitable materials for use as absorber layers in both single-junction and tandem solar cell configurations, as described by the Shockley–Queisser detailed balance limit.^[75]

Optical Properties: The optical properties of both Cu_3N and $\text{Cu}_3\text{N:S}$ were evaluated using thermo_pw. Due to incorporating sulfur into Cu_3N , the Fermi level decreased below the valence band, making it difficult to simulate the alloy since the code interprets the material as a metal. To overcome that problem, a charge of -2 was applied to the material, moving the Fermi level to the middle of the gap (Figure 3b). **Figure 6** shows the dielectric constants and absorption coefficients of Cu_3N and $\text{Cu}_3\text{N:S}$. The real part of the dielectric constant of $\text{Cu}_3\text{N:S}$ is greater than that of the other materials and does not have steep dips like Cu_3N is. For the imaginary part, Cu_3N has two peaks at ≈ 1.3 and 2 eV, whereas $\text{Cu}_3\text{N:S}$ has peaks at ≈ 2.7 and 3.6 eV. The absorption coefficient of Cu_3N starts increasing exponentially at ≈ 0.9 eV, whereas that of $\text{Cu}_3\text{N:S}$ increases slowly until 2 eV, where it starts increasing exponentially, and that is what is expected since $\text{Cu}_3\text{N:S}$ has a wider bandgap. We performed calculations of the intrinsic Cu_3N with Hubbard (Figure S2, Supporting Information) to account for the underestimation of the bandgap, and the results coincide with the experimental results of Matsuzaki et al.^[3]

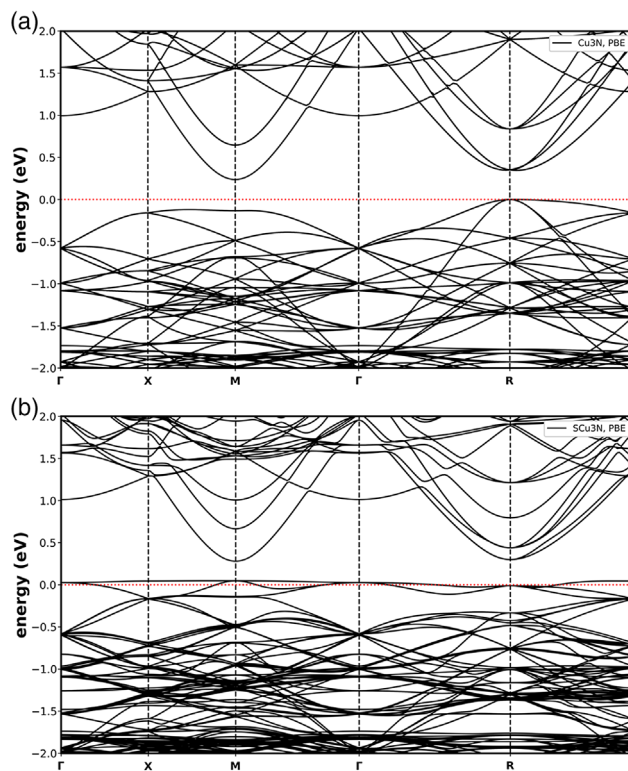


Figure 7. Band structure of pure Cu_3N and sulfur-doped Cu_3N in the supercell configuration: a) pure Cu_3N and b) sulfur-doped Cu_3N .

Table 5. Bandgap distances at different symmetry points for $3 \times 3 \times 3$ Cu_3N doped with sulfur. Values with Hubbard are calculated using $U = 7.64$ eV.

$3 \times 3 \times 3$	M–M	R–R	R–M	G–G	G–M	G–R	X–M	X–R	M–R
$\text{Cu}_3\text{N}:\text{S}$	0.2319	0.3106	0.2909	0.9863	0.2532	0.2729	0.2349	0.2546	0.2516
$\text{Cu}_3\text{N}:\text{S}$ –Hubbard	0.7349	1.0873	0.9958	1.2360	0.7726	0.8641	0.7241	0.8156	0.8264

3.3.2. Supercell

An enlarged unit cell that replicates the crystal lattice is called a supercell in DFT calculations and is used to examine materials more precisely, including defects or impurities. This section presents the analysis of a $3 \times 3 \times 3$ supercell of Cu_3N .

Band Structure: Band structure simulations in the literature were performed using a single cell for Cu_3N . In this study, supercell calculations were conducted for pure Cu_3N and sulfur-doped Cu_3N to compare and identify the effect of doping with sulfur. To the best of our knowledge, no one has performed a $3 \times 3 \times 3$ band structure calculation for Cu_3N . Surprisingly, the results in **Figure 7a** indicate that the material has a narrower R–R and M–M direct bandgap than the single-cell calculation. Sometimes, Perdew–Burke–Ernzerhof (PBE) calculations have reported that PBE behaves strangely in varying cell configurations. Hybrid functional calculations for supercells were not performed due to the prohibitive computational cost. Instead, Hubbard calculations were made for reference (**Figure S3** and **S4**, Supporting Information). The PBE results for pure Cu_3N single-cell direct bandgaps are 0.837 and 0.931 eV; for the supercell, they are 0.352 and 0.371 eV for R–R and M–M, respectively. Incorporating sulfur into Cu_3N results in degenerate p-type doping, as shown in **Figure 7b**; a similar result was obtained by Sahoo et al.^[73]

Interestingly, the valance band increased in intensity when doped with sulfur. **Table 5** summarizes the bandgaps at different symmetry points. The incorporation of sulfur changes the material to a direct bandgap material with a bandgap of 0.232 eV at the M–M point.

Conductivity and Power Factor: Conductivity and power factor (PF) calculations were performed using BoltzTraP. A summary of the results for the conductivity and PFs is presented in **Table 6** and **7**, respectively, and all the results are at 300 K. As shown in the tables, the incorporation of sulfur improved the conductivity of Cu_3N by two orders of magnitude, which could result in better performance of the Cu_3N devices. Similarly, doping improved the PF by approximately two orders of magnitude.

3.4. Thermal Properties

The thermal properties of doped and undoped Cu_3N were determined in this study. One method for determining a material's conductivity type is to determine the Seebeck coefficient. A positive Seebeck coefficient means that the material is a p-type material, and a negative Seebeck coefficient implies that it is an n-type material. **Table 2** summarizes the Seebeck coefficients of the different planes for both the doped and undoped Cu_3N . Based on our DFT simulation, undoped Cu_3N has a negative Seebeck

Table 6. Conductivity of doped and undoped $3 \times 3 \times 3$ Cu_3N supercells at 300 K at the Fermi level.

$3 \times 3 \times 3$	S_{xx} [$\text{W}^{-1} \text{m}^{-1} \text{s}^{-1}$]	S_{yy} [$\text{W}^{-1} \text{m}^{-1} \text{s}^{-1}$]	S_{zz} [$\text{W}^{-1} \text{m}^{-1} \text{s}^{-1}$]
Cu_3N	5.80×10^{16}	5.80×10^{16}	5.80×10^{16}
$\text{Cu}_3\text{N}:\text{S}$	5.85×10^{18}	5.85×10^{18}	5.85×10^{18}

Table 7. PF of the doped and undoped $3 \times 3 \times 3$ Cu_3N supercell at 300 K at the Fermi level.

$3 \times 3 \times 3$	PF_{xx} [$\text{Wm}^{-1} \text{K}^{-2} \text{s}^{-1}$]	PF_{yy} [$\text{Wm}^{-1} \text{K}^{-2} \text{s}^{-1}$]	PF_{zz} [$\text{Wm}^{-1} \text{K}^{-2} \text{s}^{-1}$]
Cu_3N	9.17×10^8	9.17×10^8	9.17×10^8
$\text{Cu}_3\text{N}:\text{S}$	6.77×10^{10}	6.77×10^{10}	6.77×10^{10}

coefficient of -2.33 mV K^{-1} , which means that pure Cu_3N is an n-type material. However, when doped with sulfur at the interstitial site, the material turned into a p-type material with a positive Seebeck coefficient value of 107.59 mV K^{-1} .

On the other hand, the Seebeck coefficient is negative for sulfur at the nitrogen site, resulting in an n-type material. Moreover, the thermal conductivities of both doped and undoped Cu_3N were determined. Since the most likely doping site based on the formation energy indicates that sulfur will be in the interstitial site, we only performed thermal conductivity calculations for interstitial doping. The thermal conductivity of undoped Cu_3N was found to be $6.27 \times 10^{12} \text{ Wm}^{-1} \text{K}^{-1} \text{s}^{-1}$, and when doped with sulfur, it increased by approximately four times— $24.64 \times 10^{12} \text{ Wm}^{-1} \text{K}^{-1} \text{s}^{-1}$ —to be precise. Thus, doping with sulfur positively impacts the thermal properties of Cu_3N .

4. Conclusion

The structural, electronic, optical, and thermal properties of pure Cu_3N and sulfur doped Cu_3N were examined in this DFT study utilizing different DFT algorithms. The sulfur incorporation increased the lattice constant by 0.136 Å, transforming Cu_3N into a new softer material with a higher bandgap. The dielectric constant and absorption coefficient change dramatically due to alloying. On the other hand, this analysis revealed the favorable interstitial position for sulfur doping out of interstitial, nitrogen, face, and copper positions, and highlighted the material's transition from intrinsic n-type to p-type behavior, which is evident in the altered Seebeck coefficient. The incorporation of sulfur into the Cu_3N supercell improved the electrical and thermal properties of Cu_3N . Surprisingly, the band structure of the Cu_3N supercell showed lower bandgaps (M–M and R–R) than did those of

the single-cell results. Furthermore, the band structure of the doped specimen shows a flat valence band and a further reduction in the material's bandgaps, which, in turn, should lead to an increase in the optical absorption of the material, which is relevant to solar cell and photodetector applications. The electrical conductivity and PF of $\text{Cu}_3\text{N:S}$ increased remarkably by two orders of magnitude, emphasizing its superior performance. Furthermore, the thermal conductivity exhibited a significant fourfold increase, indicating enhanced thermal properties. This research underscores the material's promise for solar cell technology, as it offers superior electrical and thermal properties that could advance sustainable energy applications.

Supporting Information

Supporting Information is available from the Wiley Online Library or from the author.

Acknowledgements

The authors thank the Ohio Supercomputer Center (OSC) for access to its computational resources via project PJS0339.

Conflict of Interest

The authors declare no conflict of interest.

Author Contributions

Md Maidul Islam, Sajjad A. Alqunais, Daniel G. Georgiev: Conceptualization. **Sajjad A. Alqunais, Md Maidul Islam, B. B. Dumre, Daniel G. Georgiev:** Methodology. **Sajjad A. Alqunais:** Computation. **Sajjad A. Alqunais, Md Maidul Islam, B. B. Dumre, Daniel G. Georgiev:** Data analysis. **Sajjad A. Alqunais, Md Maidul Islam, B. B. Dumre:** Writing. **Md Maidul Islam, B. B. Dumre, Daniel G. Georgiev, S. V. Khare:** Review and editing. **Daniel G. Georgiev, S. V. Khare:** Funding acquisition. **Daniel G. Georgiev:** Supervision. All authors have read and agreed to the published version of the manuscript.

Data Availability Statement

The data that support the findings of this study are available on request from the corresponding author. The data are not publicly available due to privacy or ethical restrictions.

Keywords

Cu_3N , density functional theory, interstitial position, P-type doping, sulfur

Received: July 5, 2024

Revised: September 18, 2024

Published online: October 9, 2024

- [1] K. Matsuzaki, T. Okazaki, Y.-S. Lee, H. Hosono, T. Susaki, *Appl. Phys. Lett.* **2014**, *105*, 222102.
[2] A. N. Fioretti, C. P. Schwartz, J. Vinson, D. Nordlund, D. Prendergast, A. C. Tamboli, C. M. Caskey, F. Tuomisto, F. Linez, S. T. Christensen, E. S. Toberer, S. Lany, A. Zakutayev, *J. Appl. Phys.* **2016**, *119*, 181508.

- [3] K. Matsuzaki, K. Harada, Y. Kumagai, S. Koshiya, K. Kimoto, S. Ueda, M. Sasase, A. Maeda, T. Susaki, M. Kitano, F. Oba, H. Hosono, *Adv. Mater.* **2018**, *30*, 1801968.
[4] S.-C. Chen, S.-Y. Huang, S. Sakalley, A. Paliwal, Y.-H. Chen, M.-H. Liao, H. Sun, S. Biring, *J. Alloys Compd.* **2019**, *789*, 428.
[5] C. Navío, M. J. Capitán, J. Álvarez, F. Yndurain, R. Miranda, *Phys. Rev. B* **2007**, *76*, 085105.
[6] Y. S. Yee, H. Inoue, A. Hultqvist, D. Hanifi, A. Salleo, B. Magyariköpe, Y. Nishi, S. F. Bent, B. M. Clemens, *Phys. Rev. B* **2018**, *97*, 245201.
[7] S. Sakalley, A. Saravanan, W.-C. Cheng, S.-C. Chen, H. Sun, C.-L. Hsu, B.-R. Huang, *J. Alloys Compd.* **2022**, *896*, 162924.
[8] D. M. Borsa, S. Grachev, C. Presura, D. O. Boerma, *Appl. Phys. Lett.* **2002**, *80*, 1823.
[9] D. Wang, N. Nakamine, Y. Hayashi, *J. Vac. Sci. Technol., A* **1998**, *16*, 2084.
[10] J. Xiao, M. Qi, C. Gong, Z. Wang, A. Jiang, J. Ma, Y. Cheng, *J. Phys. D: Appl. Phys.* **2018**, *51*, 055305.
[11] A. Jiang, J. Xiao, C. Gong, Z. Wang, S. Ma, *Vacuum* **2019**, *164*, 53.
[12] L. Zhu, X. Cao, C. Gong, A. Jiang, Y. Cheng, J. Xiao, *Materials* **2020**, *13*, 1873.
[13] J. Xiao, M. Qi, Y. Cheng, A. Jiang, Y. Zeng, J. Ma, *RSC Adv.* **2016**, *6*, 40895.
[14] M. M. Islam, D. G. Georgiev, *Appl. Phys. A* **2022**, *128*, 579.
[15] A. Jiang, M. Qi, J. Xiao, *J. Mater. Sci. Technol.* **2018**, *34*, 1467.
[16] M. I. Rodríguez-Tapiador, J. M. Asensi, M. Roldán, J. Merino, J. Bertomeu, S. Fernández, *Coatings* **2023**, *13*, 1094.
[17] A. Ścigała, E. Szlyk, L. Dobrzańska, D. H. Gregory, R. Szczepny, *Coord. Chem. Rev.* **2021**, *436*, 213791.
[18] T. Xu, Z. X. Cao, A. L. Ji, *J. Alloys Compd.* **2016**, *685*, 423.
[19] J. Yang, S. Huang, Z. Wang, Y. Hou, Y. Shi, J. Zhang, J. Yang, X. Li, *J. Vac. Sci. Technol., A* **2014**, *32*, 051510.
[20] Y. Zhao, Q. Zhang, S. Huang, J. Zhang, S. Ren, H. Wang, L. Wang, T. Yang, J. Yang, X. Li, *J. Supercond. Novel Magn.* **2016**, *29*, 2351.
[21] A. Jiang, H. Shao, L. Zhu, S. Ma, J. Xiao, *Materials* **2020**, *13*, 4325.
[22] H.-H. He, X.-L. Qiu, B.-C. Gong, Z.-Y. Lu, K. Liu, *Phys. Rev. B* **2023**, *108*, 115147.
[23] Z. Wu, H. Chen, N. Gao, J. Yang, T. Yang, J. Zhang, X. Li, K. Yao, *Solid State Commun.* **2015**, *201*, 9.
[24] A. Fallberg, M. Ottosson, J.-O. Carlsson, *J. Cryst. Growth* **2010**, *312*, 1779.
[25] G. Sahoo, *Mater. Today Commun.* **2021**, *29*, 102950.
[26] G. Sahoo, A. Jena, *Mater. Today Commun.* **2022**, *33*, 104194.
[27] A. Yu, R. Hu, W. Liu, R. Zhang, J. Zhang, Y. Pu, L. Chu, J. Yang, X. Li, *Curr. Appl. Phys.* **2018**, *18*, 1306.
[28] H. Noh, H. An, J. Lee, J. Song, H. J. Hong, S. Seo, S. Y. Jeong, B.-J. Kim, S. Ryu, S. Lee, *J. Korean Ceram. Soc.* **2020**, *57*, 345.
[29] X. Y. Cui, A. Soon, A. E. Phillips, R. K. Zheng, Z. W. Liu, B. Delley, S. P. Ringer, C. Stampfl, *J. Magn. Magn. Mater.* **2012**, *324*, 3138.
[30] K. Matsuzaki, T. Katase, T. Kamiya, H. Hosono, *ACS Appl. Mater. Interfaces* **2019**, *11*, 35132.
[31] A. Usikov, O. Kovalenkov, V. Soukhoveev, V. Ivantsov, A. Syrkin, V. Dmitriev, A. Y. Nikiforov, S. G. Sundaresan, S. J. Jeliakzov, A. V. Davydov, *Phys. Status Solidi C* **2008**, *5*, 1829.
[32] Information NCFB. PubChem Compound Summary for CID 24553, Nitrogen trifluoride.
[33] A. Tilemachou, M. Zervos, A. Othonos, T. Pavloudis, J. Kioseoglou, *Electron. Mater.* **2022**, *3*, 15.
[34] J. L. Lyons, A. Janotti, C. G. Van De Walle, *Phys. Rev. B* **2014**, *89*, 035204.
[35] A. L. Allred, E. G. Rochow, *J. Inorg. Nucl. Chem.* **1958**, *5*, 264.
[36] P. Giannozzi, O. Andreussi, T. Brumme, O. Bunau, M. Buongiorno Nardelli, M. Calandra, R. Car, C. Cavazzoni, D. Ceresoli, M. Cococcioni, N. Colonna, I. Carnimeo, A. Dal Corso, S. de Gironcoli, P. Delugas, R. A. DiStasio Jr, A. Ferretti, A. Floris,

- G. Fratesi, G. Fugallo, R. Gebauer, U. Gerstmann, F. Giustino, T. Gorni, J. Jia, M. Kawamura, H.-Y. Ko, A. Kokalj, E. Küçükbenli, A. Lazzeri, M. Marsili, et al. *J. Phys.: Condens. Matter* **2017**, *29*, 465901.
- [37] P. Giannozzi, S. Baroni, N. Bonini, M. Calandra, R. Car, C. Cavazzoni, D. Ceresoli, G. L. Chiarotti, M. Cococcioni, I. Dabo, A. Dal Corso, I. Carnimeo, A. Dal Corso, S. de Gironcoli, S. Fabris, G. Fratesi, R. Gebauer, U. Gerstmann, C. Gougoussis, A. Kokalj, M. Lazzeri, L. Martin-Samos, N. Marzari, F. Mauri, R. Mazzarello, S. Paolini, A. Pasquarello, L. Paulatto, C. Sbraccia, S. Scandolo, G. Sclauzero, et al., *J. Phys.: Condens. Matter* **2009**, *21*, 395502.
- [38] A. D. Corso, Welcome to Thermo_pw.
- [39] G. K. H. Madsen, D. J. Singh, *Comput. Phys. Commun.* **2006**, *175*, 67.
- [40] G. Prandini, A. Marrazzo, I. E. Castelli, N. Mounet, N. Marzari, *NPJ Comput. Mater.* **2018**, *4*, 72.
- [41] K. Balasubramanian, S. V. Khare, D. Gall, *Acta Mater.* **2018**, *159*, 77.
- [42] B. D. Ozsdolay, C. P. Mulligan, K. Balasubramanian, L. Huang, S. V. Khare, D. Gall, *Surface Coat. Technol.* **2016**, *304*, 98.
- [43] K. Zhang, K. Balasubramanian, B. D. Ozsdolay, C. P. Mulligan, S. V. Khare, W. T. Zheng, D. Gall, *Surf. Coat. Technol.* **2015**, *277*, 136.
- [44] K. Zhang, K. Balasubramanian, B. D. Ozsdolay, C. P. Mulligan, S. V. Khare, W. T. Zheng, D. Gall, *Surf. Coat. Technol.* **2016**, *288*, 105.
- [45] I. Efthimiopoulos, I. Khatri, Z. T. Y. Liu, S. V. Khare, P. Sarin, V. Tsurkan, A. Loidl, D. Zhang, Y. Wang, *Phys. Rev. B* **2018**, *97*, 184435.
- [46] V. Adhikari, N. J. Szymanski, I. Khatri, D. Gall, S. V. Khare, *Thin Solid Films* **2019**, *688*, 137284.
- [47] Z. T. Y. Liu, B. P. Burton, S. V. Khare, D. Gall, *J. Phys: Condens. Matter* **2017**, *29*, 035401.
- [48] Z. T. Y. Liu, N. J. Podraza, S. V. Khare, P. Sarin, *Comput. Mater. Sci.* **2018**, *144*, 139.
- [49] I. Khatri, N. J. Szymanski, B. B. Dumre, J. G. Amar, D. Gall, S. V. Khare, *J. Alloys Compd.* **2021**, *891*, 161866.
- [50] B. Wang, M. Zhang, V. Adhikari, P. Fang, S. V. Khare, D. Gall, *J. Mater. Chem. C* **2020**, *8*, 12677.
- [51] N. J. Szymanski, I. Khatri, J. G. Amar, D. Gall, S. V. Khare, *J. Mater. Chem. C* **2019**, *7*, 12619.
- [52] N. J. Szymanski, L. N. L. Walters, O. Hellman, D. Gall, S. V. Khare, *J. Mater. Chem. A* **2018**, *6*, 20852.
- [53] A. W. Ghosh, S. V. Khare, *Phys. Rev. Lett.* **2000**, *84*, 5243.
- [54] J. L. Roehl, A. Kolagatla, V. K. K. Ganguri, S. V. Khare, R. J. Phaneuf, *Phys. Rev. B* **2010**, *82*, 165335.
- [55] K. Balasubramanian, S. Khare, D. Gall, *Phys. Rev. B* **2016**, *94*, 174111.
- [56] J. L. Roehl, S. V. Khare, *Solar Energy* **2014**, *101*, 245.
- [57] J. L. Roehl, S. V. Khare, *Sol. Energy Mater. Sol. Cells* **2014**, *128*, 343.
- [58] J. L. Roehl, Z. T. Y. Liu, S. V. Khare, *Mater. Res. Express* **2014**, *1*, 025904.
- [59] J. A. Warner, S. K. R. Patil, S. V. Khare, K. C. Masiulaniec, *Appl. Phys. Lett.* **2006**, *88*, 101911.
- [60] X. Zhou, D. Gall, S. V. Khare, *J. Alloys Compd.* **2014**, *595*, 80.
- [61] M. Zervos, A. Othonos, M. Sergides, T. Pavloudis, J. Kioseoglou, *J. Phys. Chem. C* **2020**, *124*, 3459.
- [62] N. J. Szymanski, V. Adhikari, M. A. Willard, P. Sarin, D. Gall, S. V. Khare, *J. Appl. Phys.* **2019**, *126*, 093903.
- [63] N. J. Szymanski, Z. T. Y. Liu, T. Alderson, N. J. Podraza, P. Sarin, S. V. Khare, *Comput. Mater. Sci.* **2018**, *146*, 310.
- [64] V. Adhikari, Z. T. Y. Liu, N. J. Szymanski, I. Khatri, D. Gall, P. Sarin, S. V. Khare, *J. Phys. Chem. Solids* **2018**, *120*, 197.
- [65] I. S. Khare, N. J. Szymanski, D. Gall, R. E. Irving, *Comput. Mater. Sci.* **2020**, *183*, 109818.
- [66] A. Mascarenhas, Y. Zhang, J. Verley, M. J. Seong, *Superlattices Microstruct.* **2001**, *29*, 395.
- [67] F. Birch, *Phys. Rev.* **1947**, *71*, 809.
- [68] H. Chen, X. Li, J. Zhao, Z. Wu, T. Yang, Y. Ma, W. Huang, K. Yao, *Comput. Theor. Chem.* **2013**, *1018*, 71.
- [69] H. Chen, X. Li, J. Zhao, Z. Wu, T. Yang, Y. Ma, W. Huang, K. Yao, *Comput. Theor. Chem.* **2014**, *1027*, 33.
- [70] M. G. Moreno-Armenta, W. L. Pérez, N. Takeuchi, *Solid State Sci.* **2007**, *9*, 166.
- [71] A. Rahmati, M. Ghoolestani, H. Badehian, M. Baizae, *Mater. Res.* **2014**, *17*, 303.
- [72] M. Zervos, A. Othonos, T. Pavloudis, S. Giaremis, J. Kioseoglou, K. Mavridou, M. Katsikini, F. Pinakidou, E. C. Paloura, *J. Phys. Chem. C* **2021**, *125*, 3680.
- [73] G. Sahoo, R. Kashikar, M. K. Jain, B. R. K. Nanda, *Mater. Res. Express* **2016**, *3*, 065902.
- [74] S. Li, J. Hao, S. Yu, *Vacuum* **2021**, *191*, 110366.
- [75] W. Shockley, H. J. Queisser, *J. Appl. Phys.* **1961**, *32*, 510.
- [76] K. Momma, F. Izumi, *J. Appl. Crystallogr.* **2008**, *41*, 653.